Article

Key propagation pathways of extreme precipitation events revealed by climate networks

Check for updates

Kaiwen Li[1,2,3], Yu Huang [3,4], Kai Liu[1,5], Ming Wang [1,5 ✉], Fenying Cai [3], Jianxin Zhang [1,3,6] & Niklas Boers [3,4]

The comprehensive understanding of propagation patterns of extreme precipitation events (EPEs) is essential for early warning of associated hazards such as floods and landslides. In this study, we utilize climate networks based on an event synchronization measure to investigate the propagation patterns of EPEs over the global land masses, and identify 16 major propagation pathways. We explain them in association with regional weather systems, topographic effects, and travelling Rossby wave patterns. We also demonstrate that the revealed propagation pathways carry substantial EPE predictability in certain areas, such as in the Appalachian, the Andes mountains. Our results help to improve the understanding of key propagation patterns of EPEs, where the global diversity of the propagated patterns of EPEs and corresponding potential predictability provide prior knowledge for predicting EPEs, and demonstrate the power of climate network approaches to study the spatiotemporal connectivity of extreme events in the climate system.

Extreme precipitation events (EPEs) have substantial impacts on human society and economy[1]. For example, extreme precipitation puts severe pressure on urban sewage treatment networks[2] and contributes to outbreaks of waterborne diseases[3]. Natural hazards triggered by extreme precipitation, such as floods, landslides, or mudslides, result in devastating damage to critical infrastructure[4,5], and further lead to prolonged and adverse impacts on economic activities[6–8]. The increasing magnitude and frequency of EPEs caused by global warming[9,10] have raised substantial public concerns in the past few decades. Research related to extreme precipitations has been carried out extensively, where advanced deep learning frameworks have been utilized to effectively extract and learn complex features and patterns from large-scale meteorological data, substantially improving our understanding of extreme precipitation and bringing high prediction skills[11,12]. However, exploring the propagation patterns of EPEs and uncovering the mechanisms behind them remains a challenge.

Climate networks have been widely applied as a powerful tool for the study of EPEs and associated teleconnections[13–16]. For example, Boers et al. introduced a method combining event synchronization (ES) with climate networks to forecast over 60% of the EPEs in the central Andes of South America, where the travelling Rossby waves over South America were demonstrated to be the causation of the EPEs' synchronization and propagation patterns[15,17]. This approach was also applied to reveal the teleconnection patterns of global extreme precipitation[18]. Agarwal et al. have utilized ES and a similarity measure called edit distance to investigate extreme precipitation patterns in the Ganga River basin, and have identified essential locations in the river basin with respect to potential prediction skill of EPEs[19]. Approaches based on ES and climate networks have also helped revealing the propagation characteristics of extreme summer precipitation in the United States[20] and the synchronization pattern of extreme precipitation in Easter Asia[21,22]. The current research suggests that there exist preferred spatiotemporal patterns associated with the occurrence of EPEs, but to our knowledge the information provided by the literature primarily focuses on the precipitation coherence phenomenon under the specific local weather systems, or limited to a specific region. A comparative investigation on the EPEs across diverse global regions is lacking. Mostly the community would be interested in the cases over other regions, and how the different regions are different from one another. This has not been thoroughly explored previously, thus holds considerable value for further investigation.

Here, we establish and evaluate a global directed network of EPEs over the global land and investigate potential preferred propagation pathways of

[1]School of National Safety and Emergency Management, Beijing Normal University, Beijing, China. [2]Faculty of Geographical Science, Beijing Normal University, Beijing, China. [3]Department of Complexity Science, Potsdam Institute for Climate Impact Research (PIK), Potsdam, Germany. [4]Earth System Modelling, School of Engineering & Design, Technical University of Munich, Munich, Germany. [5]Joint International Research Laboratory of Catastrophe Simulation and Systemic Risk Governance, Beijing Normal University at Zhuhai, Zhuhai, China. [6]School of Systems Science, Beijing Normal University, Beijing, China. ✉e-mail: wangming@bnu.edu.cn

1

EPEs on different continents, using ES in combination with climate networks. The physical mechanisms of the revealed propagation pathways are then verified from the perspectives of travelling Rossby waves in interplay with topography. Furthermore, we analyze the potential predictability of EPEs at different locations along their propagation pathways.

Results

Global climate network analysis of EPEs over land

The similarity measure ES quantifies the co-occurrence of extreme events in a pair of time series with a dynamical time lag[23]. This enables us to depict the synchronization between EPEs at different locations over the global land masses (Methods section 'Event synchronization').

A functional climate network is defined as a directed graph, in which nodes represent global land grid cells, edge weights reflect the strength of ES. For direction attributes, if the direction is from grid cell i (j) to grid cell j (i), it indicates that EPEs at grid cell i typically occur before (after) those at grid cell j. Upon applying suitable significance tests and pruning edges, a climate network for EPEs is obtained, where network edges are placed whenever corresponding ES values are significant with $p < 0.01$ (Methods section 'Functional climate networks' and 'Significance tests'). The sensitivity of the climate network to varying the different parameters used for network construction - such as the p-value above - reflects the robustness of the patterns revealed by the network metrics. Therefore, we compare the geographical distance distribution of the EPEs' climate network with maximum delay $\tau_{max} = 3, 6, 10$ days (Supplementary Fig. 1; Methods section 'Robustness tests'). The statistics of network edges' geographical distances follow a consistent power-law distribution when setting different τ_{max}, suggesting that the established climate network here is of great robustness. It is also noted that there are much less synchronization effects for edges with longer distances than that with shorter distances.

For this EPEs network, the edges with a short distance are considered, in line with the interpretation given in[15], as corresponding to regional weather systems, while the edges with a long distance, say longer than 1000 km, may be associated with global large-scale circulation patterns[18]. Previous work has demonstrated that the global distribution of spatial distances of synchronized links decays as the power law at distances lower than 2500 km, but exhibits a super-power-law behavior at greater distances. The links associated with regional weather systems with distances up to 2500 km, including mesoscale convective systems and tropical cyclones, the remaining links are related to atmospheric teleconnection patterns[18,22]. We therefore use this distance to define the short-distance network (i.e., the inner edge distances are less than 2500 km) here. The network-based statistics hereafter are all based on this short-distance network. Regional weather systems, such as frontal systems or convective systems in the (sub)tropics, promote the propagation of extreme precipitation by creating opportunities for lifting airflow and moisture transport[24,25]. To quantitatively identify the propagation pathways of the EPEs, the network

divergence is introduced to determine the source and sink regions[15,20] of the EPEs propagation (Fig. 1b; see Methods section 'Functional climate networks'). Here, sources and sinks in the network represent the start and end of propagating events within a specific regional weather system. Clear source and sink regions can be observed in North America, South America, and Australia. The spatial distribution of network divergence in North America, Europe, and Australia exhibits a West-East-coast pattern, i.e., the western part of the continent generally has a positive network divergence, the eastern side has a negative network divergence, suggesting that the western part of the continent is more likely to be the sources for the dynamics of EPEs, while the eastern side is the sinks. The propagation of EPEs requires adequate moisture conditions and anomalous pressure systems. Previous studies have shown that the main mechanisms of moisture transport on a global scale: Low-Level Jets, atmospheric rivers, and monsoon systems carry substantial moisture from tropical oceans moving from west to east, and provide moisture conditions for the formation of EPEs after arriving on land[26]. For example, the Pineapple Express in North America[27], the West African westerly jet[28], and the coupling of the eastward movement of the Rossby waves with the Low-Level Jets have also been linked to the synchronization of precipitation extremes in mid-latitudes[17,29]. In summary, the western part of the continents of North America, Europe, and Australia are more likely to receive moisture from tropical oceans and to form sources under the influence of the eastward travelling of Rossby waves, while the eastern part of the continent are more likely to be sinks, resulting in the West-East-coast pattern. Compared to the Southern Hemisphere, the absolute value of network divergence ΔS in the Northern Hemisphere is higher. This phenomenon is attributed to the greater number of nodes over the Northern Hemispheric land, resulting in a higher count of edges; the results shown in the following are not sensitive to this effect.

Preferred propagation pathways of EPEs

The formation and propagation of EPEs under regional weather systems may be traced efficiently using climate networks. The dominant pathways are typically closely related to topography and, in the tropics and subtropics, to the development of Mesoscale Convective Systems. For example, the northward propagating frontal systems in South America collide with warm, moist air masses from the Amazon basin causing propagation of EPEs from southern-central South America toward the eastern slopes of the central Andes[15,30-32], where orographic lifting effects further increase the EPEs magnitude.

Here we identify propagation patterns of the EPEs by the divergence of the short-distance network. Taking North America as an example, we select three source regions of the EPEs network (corresponding to the typical start point of the EPEs propagation pathway)[15,33], denoted as regions A, B, and C in Fig. 2a, located in the northwestern, northeastern, and southern regions of North America. All of these are regions with notable positive network divergence and are surrounded by a distinct network sink region. We further
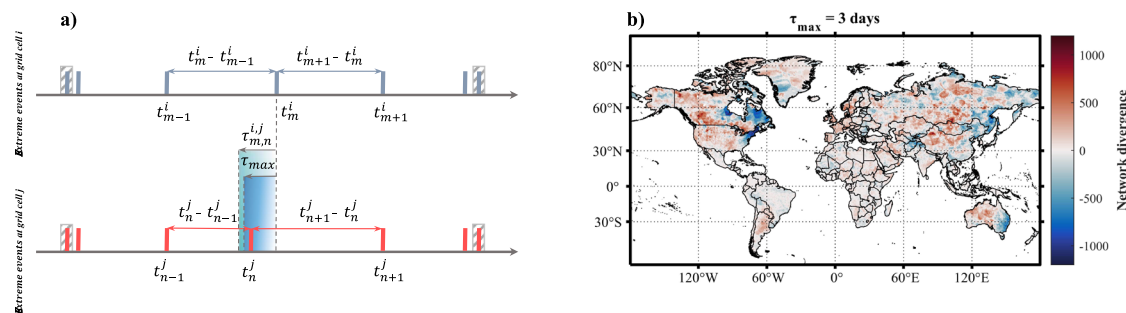
Fig. 1 | Schematic illustration of the Event Synchronization measure and the spatial distribution of network divergence in the short-distance network with $\tau_{max} = 3$ days. a Shown are a pair of extreme events series and exemplary illustrations of the dynamical delay $\tau_{m,n}^{i,j}$ and maximum delay τ_{max}. **b** Positive values of network divergence ΔS indicate source regions of the short-distance network, which

are interpreted as locations where synchronized extreme precipitation occurs within 3 days before it occurs at other locations. On the other hand, negative values indicate sink regions, that is, locations where synchronized extreme precipitation occurs within 3 days after it occurs at other locations.
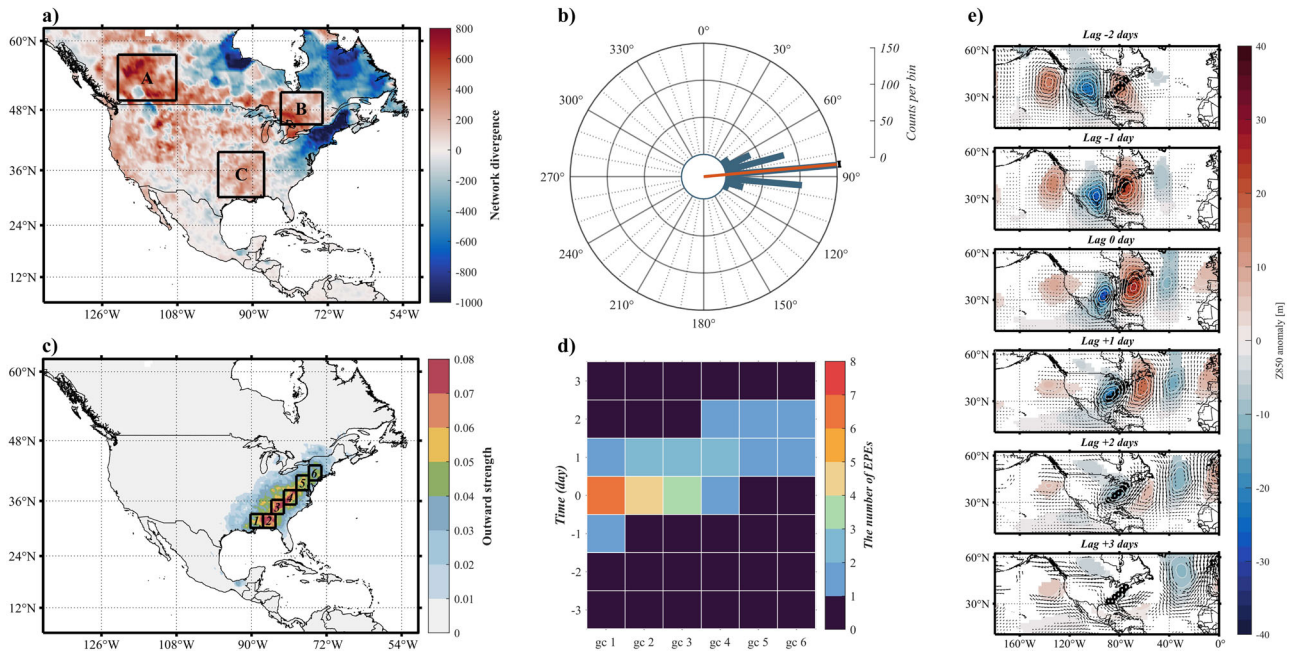
Fig. 2 | Results of the network analysis and atmospheric conditions for propagation of extreme precipitation events in region C of North America. a The spatial distribution of network divergence ΔS in North America. Regions A, B, C, marked by black boxes, are identified as the network's source regions in North America. **b** The statistical weighted mean azimuth of all grid cells in region C. The orange solid line shows the average angle and the black curve gives a 95% confidence interval for the statistical weighted mean azimuth. **c** Outward strength of region C, which is the average Out-Strength restricted to region C. Note in particular the high values along the Appalachian Mountains. **d** Spatiotemporal evolution of extreme precipitation events from region C along the sequence of boxes indicated in (**c**), where grid cell is abbreviated as gc. Composite numbers of extreme precipitation events in the respective boxes are displayed for the 3 days before and after extreme precipitation occurs at grid cell 1. Each box has an edge length of 3°. **e** Composite anomalies of 850 mb geopotential height and wind fields from NCEP-NCAR Reanalysis 1 for 2 days before to 3 days after extreme precipitation occurs at grid cell 1. Temporal resolution is daily, spatial resolution is 2.5° × 2.5°. Geopotential height contours are depicted as white curves. Only significant values in student's t-test (significance level: 0.05) are shown in the maps.

count the weighted mean azimuth of the nodes within source region C (Fig. 2b), which shows that most of the nodes exhibit stronger outward synchronization effects in the eastern part of North America (Methods section 'Functional climate networks'). In addition, outward strength of source region is introduced to identify the temporal order and dynamics of the EPEs (Methods section 'Functional climate networks'). Through calculating the spatially averaged ES values from region C to each grid cell, we note the high values of outward strength from region C extend along the Appalachian Mountains, which indicates that EPEs in region C are followed by EPEs along a narrow band along the Appalachian Mountains toward the northeastern United States. Meanwhile, five grid cells with an edge length of 3° are selected to represent the propagation pathways of EPEs from region C to the northeastern United States, considering the statistical results of the weighted mean azimuth (Fig. 2c). A strong synchronization effect is observed between the different grid cells along the propagation pathways for region C. For a certain regional weather system, the EPEs between grid cells occur with time intervals within 2 days on average (Fig. 2d). To investigate the underlying mechanism of atmospheric dynamics, we extract the time points at grid cell 1 where at least one extreme precipitation event occurs and calculate the composite anomalies of 850 mb geopotential height and wind fields for 2 days before to 3 days after the time of EPEs occurrence (Fig. 2e). The composites exhibit eastward movement of high- and low- pressure anomalies originating from Rossby wave activity, which favors the formation and propagation of the EPEs. The eastward movement of low-pressure anomalies also promotes the eastward extension of the Great Plains Low-Level Jet (GPLLJ), thereby enhancing the moisture transport from the Gulf of Mexico towards the eastern part of North America[34]. Combined with the orographic lifting effects, this ultimately leads to the formation of the revealed EPEs propagation pathway along the Appalachian Mountains.

Based on this framework, we further identify two propagation pathways of EPEs from southwestern Canada to Hudson Bay Coastal Plain and

from southeastern Canada along the Laurentian Mountains extending to the Labrador Peninsula, respectively (Supplementary Figs. 2 and 3). Previous studies have shown that synoptic moisture propagation over western and eastern Canada is associated with Rossby waves[35]. The travelling Rossby waves contribute to the formation of these two propagation pathways.

Similar EPEs propagating patterns also exist in other continents, here we furthermore present a case in Oceania. In Fig. 3a, three sub-regions in northwest, central, and southern Australia are identified as the network's source regions A, B, and C, which is closed to the coastline. The network nodes within region C almost consistently exhibit stronger outward synchronization effects in southeastern Australia, i.e., the southern part of the Great Dividing Range (Fig. 3b). The high values extensions of outward strength from region C are consistent with the orientation indicated by the weighted mean azimuths, where four grid cells are selected to represent propagation pathway of the EPEs spanning the southern part of the Central Plains (Fig. 3c). Furthermore, Hovmöller diagram of the EPEs reveal that the time intervals of extreme events between grid cells are typically within two days (Fig. 3d). For the coastal region of southern Australia, moisture contribution is linked to transport associated with atmospheric rivers originating from the Indian Ocean[36,37], and composite anomalies further indicate the continued eastward movement of low-pressure anomalies is the primary factor contributing to dynamics of the EPEs' propagating patterns (Fig. 3e).

For regions A, B, and C in Australia (Fig. 3a), the propagation pathways of the EPEs traverse the Western Plateau, the Australian basin (the Great Artesian Basin), and the hilly terrain on the western side of the Great Dividing Range, respectively. Active Rossby wave activity and topographic effects are identified as common drivers in establishing these two pathways of EPEs (Supplementary Figs. 4 and 5). In central and western Australia, the Australian Low-Level Jet plays a crucial role in moisture's transport[38]. The eastward movement of low-pressure anomalies, in interplay with the topography, provide certain weather conditions and geographical
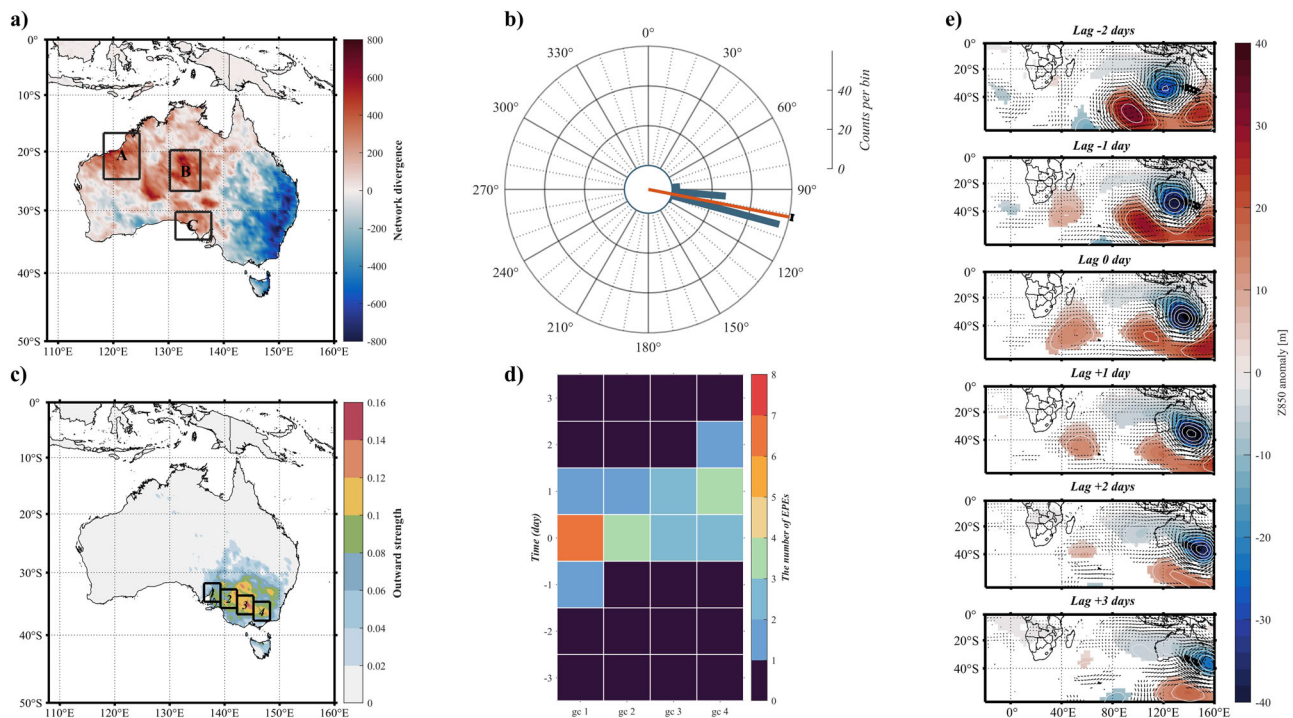
Fig. 3 | Results of the network analysis and atmospheric conditions for propagation of extreme precipitation events in region C of Australia. a The spatial distribution of network divergence ΔS in Australia. Regions A, B, C, marked by black boxes, are identified as the network's source regions in Australia. **b** The statistical weighted mean azimuth of all grid cells in region C. The orange solid line shows the average angle and the black curve gives a 95% confidence interval for the statistical weighted mean azimuth. **c** Outward strength of region C, which is the average Out-Strength restricted to region C. Note in particular the high values along the coast. **d** Spatiotemporal evolution of extreme precipitation events from region C along the sequence of boxes indicated in (**c**), where grid cell is abbreviated as gc. Composite numbers of extreme precipitation events in the respective boxes are displayed for the 3 days before and after extreme precipitation occurs at grid cell 1. Each box has an edge length of 3°. **e** Composite anomalies of 850 mb geopotential height and wind fields from NCEP-NCAR Reanalysis 1 for 2 days before to 3 days after extreme precipitation occurs at grid cell 1. Temporal resolution is daily, spatial resolution is 2.5° × 2.5°. Geopotential height contours are depicted as white curves. Only significant values in student's t-test (significance level: 0.05) are shown in the maps.

constraints for the formation of the two propagation pathways originating from regions A and B. As expected, the maximum time interval of EPEs between grid cells on longer propagation pathways is greater.

For other continents, we continued to utilize the functional climate networks to identify significant propagation patterns of EPEs. Ultimately, a total of 16 typical propagation pathways of the EPEs are detected over global lands (Fig. 4a). Most of these pathways are spatially confined by geographical features such as mountains and hills. For example, warm, moist air masses from the Amazon basin provide the potential for propagation of the EPEs from mid-latitudes to the tropics, and this propagation is proven to be associated with cold air intrusions[39,40] (Supplementary Figs. 6 and 7). In Northern Europe, the Norrland Plateau on the eastern side of the Scandinavian Mountains is leeward, and the linkage between atmospheric rivers and local precipitation extremes is weak due to the rain shadow[41]. Some studies propose that the Norrland Plateau has high skill in precipitation prediction and that regional moisture transport is mainly attributed to change in the North Atlantic Sea Surface Temperatures (SSTs) and the anticyclonic circulation over the northeastern Atlantic[42,43]. Warmer SSTs can promote more evaporation, leading to increased low-level moisture in the North Atlantic, which in combination with the influence of prevailing westerly winds and topography results in an increase in convective precipitation. The anticyclonic circulation transports moist air into Northern Europe during the summer months. The movement of low-pressure anomalies is favorable for poleward propagation of the EPEs along the eastern side of the Scandinavian Mountains[44] (Supplementary Fig. 10). Two distinct propagation pathways of EPEs are identified in Southern Europe, associated with the topography from the Iberian Peninsula to the Alps mountains and the Carpathian Mountains, respectively. The eastward movement of Rossby wave activity remains the direct cause of the propagation of EPEs (Supplementary Figs. 8 and 9). The formation of propagation pathways for EPEs follows a similar pattern in Asia and Africa (Supplementary Figs. 11–15).

Predictability of EPEs by propagation patterns

There are significant synchronization effects among EPEs at different grid cells along the propagation pathways, and we claim that this can provide a basis for early warning of floods, landslides, and other hazards caused by EPEs. To assess the potential predictability of the propagating extreme events, we employ a method based on frequency statistics, where the time when extreme events occurred at grid cell 1 is identified as the reference. By extending this reference forward for a duration of 3 days, we calculate the ratio of extreme events occurring within this time interval at subsequent grid cells to the total number of extreme events at subsequent grid cells. This result provides an estimation of the probability that an extreme event at grid cell 1 is followed by extreme events at the subsequent grid cells along the preferred propagation pathway. Note in particular the potential predictability does not equate to realized predictability, and the calculation of potential predictability only considers the occurrence of EPEs, but does not involve the intensity of EPEs. We can take the potential predictability as prior knowledge and integrate them into ensemble forecasting and machine learning forecasting in our future work to provide support for the prediction of extreme events.

Taking the case of North America (Fig. 2) as an example, the propagating patterns of the EPEs in North America typically span long geographical distances, with the probabilities of all grid cells decaying significantly with geographical distance. The three pathways

Fig. 4 | The spatial propagation pathways and predictability of extreme precipitation events.
a The 16 preferred propagation pathways of the EPEs marked by the black boxes over land. The red arrows indicate the corresponding propagation direction, the colored shading represents the global relief derived from the ETOPO1 data with a spatial resolution of 1 Arc-Minute. **b** The probability of EPEs at subsequent grid cells along the propagation pathways within 3 days after EPEs occur at grid cell 1.
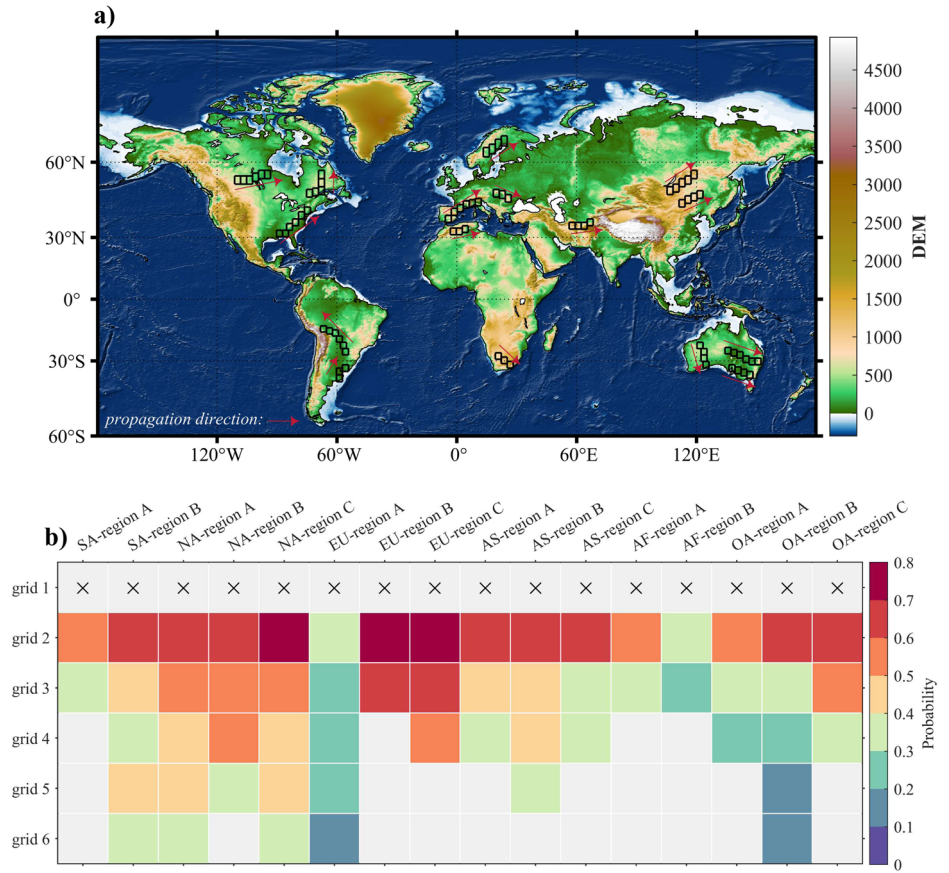
have the greatest predictive potential at grid cell 2, with an average probability of up to 68%, and still predicting more than 39% of the EPEs at the ending grid cell. In total, the average probability of the 16 preferred propagation pathways in Fig. 4b is 0.45. As the distance from the starting grid cell (i.e., grid cell 1 in Fig. 4a) increases, the probability decreases accordingly, especially for the source region C in North America and source region B in Australia. Inspecting the estimated probability metrics along different EPEs propagation pathways (Fig. 4b and Supplementary Table 1), the identified propagation patterns over North-Central Europe and North America can provide more predictable EPEs than others. Moreover, the probability clearly depends on the specific selection of the grid cells marked by spatial boxes and may be altered by adjusting their position. This is a result based on the starting point of the propagation pathways, allowing a favorable time horizon for early warning.

To further analyze the mean state and proportion of EPEs covered by the 16 preferred propagation pathways, we statistically obtain the average frequency of EPEs for each grid cell within the 16 propagation pathways, and the percentage of chain events that adhere to the corresponding propagation pattern (Supplementary Table 2). We found that for the 16 propagation pathways, on average, more than 32% of EPEs follow the propagation patterns revealed in this study. This percentage significantly exceeds the overall mean value for specific regions, such as region A in South America, region B in Europe, region C in Europe, and region C in Australia, where it reaches as high as 65.81%. The regional differences in this percentage also reflect the differences in the contribution of the revealed propagation patterns to the formation of regional precipitation extreme. Additionally, for the seasonal distributions of the above chain events, we found that chain events in North America, Europe, and Asia mainly occur during the summer and autumn, while chain events in the Southern

Hemisphere are more prevalent during winter and spring (Supplementary Fig. 16).

Discussion

We identified 16 preferred propagation pathways of EPEs and reveal significant influence of topography and atmospheric Rossby waves on the EPE propagation. The topographic lifting effect may favor the formation of particularly strong EPEs, and the continued eastward movement of low-pressure anomalies originating from Rossby wave activity embedded on the westerly jets can explain the dynamics associated with the EPE propagation patterns. Furthermore, empirical probabilities reveal the potential predictability of EPEs along the different pathways, which is valuable to provide prior knowledge for improving the forecast of EPEs. It cannot be overlooked that these important conclusions can only be draw from the comprehensive investigations on the global results. The potential predictability of EPEs may depend not only on the certain regional weather system, but is related to atmospheric teleconnections. Some studies suggest better forecast skill for extreme precipitations along the eastern side of the central Andes Mountains during warm phases of the El Niño Southern Oscillation (ENSO)[15,45,46]. The phase and amplitude of the Madden-Julian Oscillation (MJO) have been shown to modulate the probability and spatial distribution of rainfall extremes in Southeast Asia, and the convective phase of the MJO increases the probability of EPEs over land by about 30–50%[47]. The influence of atmospheric teleconnections on EPEs may be an extension of the modulation of regional weather systems by atmospheric waves. Here we found that the ENSO has weak influence on the spatial propagating pathways of EPEs, but the warm and cold ENSO phases can induce higher predictability of the propagating EPEs (not shown here). More in-depth investigation of the relationship between atmospheric teleconnections and EPE propagation pathways will be addressed in our future work.

EPEs are caused by complex processes, which normally leads to large uncertainties in modelling and predicting global EPEs with general circulation models. Our study employs the advanced climate network approaches to study EPEs, and find that there exist robust synchronization and propagation patterns of EPEs over global land, which provides promising insights for the predictability of EPEs. Also, the ordinal patterns of observational EPEs could bring a reasonable way to evaluate and improve the EPEs by climate modelling in the future study. Further, the framework proposed in this study can be also instructive for studying more problems of climate extreme events, such as the spatial propagation and forecast of heatwaves, cold waves, or air pollution.

Methods
Datasets
We utilize the National Oceanic and Atmospheric Administration (NOAA) Climate Prediction Center (CPC) Global Unified Gauge-Based Analysis of daily precipitation data for the period from 1980 to 2020 with a spatial resolution of $0.5° \times 0.5°$, and there are 360 grid cells in the north-south direction and 720 grid cells in the east-west direction. The dataset is constructed from gauge reports from over 30,000 stations collected from multiple sources, including other national and international agencies. Quality control is performed through comparisons with historical records and independent information from measurements at nearby stations, concurrent radar, satellite observations, and numerical model forecasts[48]. Optimal interpolation with orographic consideration is used to interpolate the dataset. The optimal interpolation defines the analyzed value at a grid cell by modifying a first-guess field with the weighted mean of the differences between the observed and the first-guess values at station locations within a search distance, where the weight is determined from the variance and covariance structure of the target precipitation fields[49]. Compared with existing products, the datasets show improvement in representing spatial distribution patterns and temporal changes of precipitation[50]. The Antarctic region is not considered in this study due to the sparse distribution of stations, which could lead to unstable data quality. For Meteorological variables, such as 850 mb geopotential height, and 850 mb zonal and meridional wind component obtained from the National Centers for Environmental Prediction-National Center for Atmospheric Research (NCEP-NCAR) Reanalysis 1 with a spatial resolution of $2.5° \times 2.5°$ are used in this study to derive the underlying evolution of atmospheric patterns associated with the EPEs. For geographical variables, we employ the ETOPO1 data for ice surface versions with a spatial resolution of 1 Arc-Minute. The data are derived from the ETOPO1 Global Relief Model, which integrates topographic, bathymetric, and shoreline data from regional and global datasets to enable comprehensive, high-resolution renderings of geophysical characteristics of the earth's surface[51].

The 95th percentile of the wet day (≥ 1 mm day^{-1}) for each grid cell is defined as the threshold for extreme precipitation[8,18], EPEs occurring on consecutive days are counted as one event, and the occurrence time of each extreme precipitation event is determined as the first day of occurrence.

Event synchronization
The non-linear synchronization measure ES is used to reveal preferred propagating patterns of extreme events. As shown in Fig. 1a, grid cell i and grid cell j are selected to describe the definition of synchronized events[52]. We suppose that for grid cell i, an extreme precipitation event occurs at a moment t_m^i; for grid cell j, an extreme precipitation event occurs at a moment t_n^j, where $m \in [1, M]$, $n \in [1, N]$, M and N denote the total number of EPEs at grid cells i and j, respectively. A dynamical delay $\tau_{m,n}^{i,j}$ is introduced to decide whether a pair of extreme events occurring at t_m^i and t_n^j is counted as a synchronized event, and its definition is as follows:

$$\tau_{m,n}^{i,j} = min\left(\frac{\left\{t_{m+1}^i - t_m^i, t_m^i - t_{m-1}^i, t_{n+1}^j - t_n^j, t_n^j - t_{n-1}^j\right\}}{2}\right) \quad (1)$$

Furthermore, we introduce a maximum delay τ_{max} to limit the maximum time interval between two synchronized events. We use $f(i/j)$ to denote the number of times an extreme precipitation event shortly occurs in grid cell i after it occurs in grid cell j, i.e.:

$$f(i/j) = \sum_{m=1}^{M} \sum_{n=1}^{N} S_{ij} \quad (2)$$

with

$$S_{ij} = \begin{cases} 1 & \text{if } 0 < t_m^i - t_n^j \leq min\left(\tau_{m,n}^{i,j}, \tau_{max}\right) \\ 1/2 & \text{if } t_m^i = t_n^j \\ 0 & \text{else} \end{cases} \quad (3)$$

and analogously for $f(j/i)$. q_{ij} denotes the directed synchronization strength between grid cell i and j, and its expression is given as:

$$q_{ij} = \frac{f(j/i) - f(i/j)}{\sqrt{M \times N}} \quad (4)$$

where q_{ij} is normalized to $q_{ij} \in [-1, 1]$. There is $q_{ij} = 1$ if EPEs are fully synchronized between grid cell i and j, and EPEs at grid cell i precede EPEs at grid cell j.

Compared to the static delays in the traditional linear correlation analysis, ES measures allows for dynamic delays between events, rendering it suitable for addressing non-linear temporal relationships, where typical values for the dynamical delay fall within the range of 6 to 8 in this study (Supplementary Fig. 17). Furthermore, ES can be employed to compute the average synchronization strength of EPEs between geographical source and sink regions. This will allow us to determine the preferred propagation pathways of EPEs, thereby formulating a forecast rules for extreme rainfall.

Functional climate networks
Functional climate networks are defined as networks for which each edge is placed in accordance with statistically similar synchronized behavior of the two corresponding nodes, where nodes are represented by time series of EPEs at the global land grid cells. For a pair of nodes, we assign their respective ES values as weights to the corresponding directed edges. An edge with positive ES indicates a pointing from the node where EPEs typically occur first to the node where the synchronized extreme events occur within the subsequent 3 days. The construction of the climate network transforms the original connectivity structure of the dataset into the topology of the network and thus makes it accessible.

To spatially solve the ordinal problem of EPEs, we introduce the network divergence ΔS, which is defined as the difference between outdegree k_{out} and indegree k_{in} at each node:

$$\Delta S_i = k_{out}^i - k_{in}^i \quad (5)$$

where k_{out}^i is the number of connections directed outward from the node i, k_{in}^i is the number of connections directed inward to the node i. Positive (negative) values of network divergence ΔS indicate source (sink) regions of the network. In source regions, EPEs are followed by EPEs occurred at other nodes, and in sink regions, EPEs are preceded by EPEs occurred at other nodes.

In addition, we calculate the outward strength of the selected source regions in different continents to identify the corresponding propagating patterns of EPEs:

$$S_{out}^i(R) = \frac{\sum_{j \in R} W_{ji}}{|R|} \quad (6)$$

where W_{ji} is ES matrix of the climate network. $|R|$ denotes the number of nodes contained in the selected region R. $S_{out}^i(R) = 1$ indicate a full

synchronization from each node in region R to node i.

$$\phi_i(R) = \frac{\sum_{i \in R} W_{ij} Az_{ij}}{\sum_{i \in R} W_{ij}} \qquad (7)$$

where Az_{ij} is azimuth from node i to node j.

For the selected source regions, the weighted mean azimuth of the nodes is proposed through considering the various weights of the outward edges. The weighted mean azimuths point out the orientation with stronger outward synchronization effect for the nodes, with the reference of due north and increasing clockwise. The average angle of the weighted mean azimuths provides a directional reference for finding potential propagation pathways of EPEs. However, to obtain a clear propagation pathway, outward strength is utilized to reveal regions with high synchronization effects, where regions with high outward strength spatially demonstrate possible propagation pathways of EPEs. Grid cells are typically selected along pathways with high outward strength and eventually extended to the sinks.

Significance tests

Significance tests is employed to prune the weakly correlated edges in the climate network. For each observed ES_{ij} value, a null-model distribution is obtained by computing the ES values for 1000 pairs of surrogate extreme event series with M and N uniformly and randomly distributed extreme events. The 99th percentile of the corresponding null-model distribution is determined as the significance threshold. If the observed ES_{ij} value exceeds this threshold, it indicates that ES_{ij} value has a significance level of 0.01, and these edges between node i and node j are saved in the network. In the climate network for EPEs, edges passing the significance test will have clearer propagation relations, while edges established by small- to medium-scale weather systems occurring coincidentally at different spatial locations (without persistent patterns) are typically pruned.

Robustness tests

For the climate network, the maximum delay τ_{max} may affect the structure of the network. Although previous studies find that the maximum delay τ_{max} has a weak influence on the synchronization of EPEs[18,22], the geographical distance distributions of the network with $\tau_{max} = 3, 6, 10$ days are compared in the Supplementary Materials because our study investigates the extreme precipitation synchronization between global land grid cells.

Data availability

CPC daily precipitation data is freely available from the NOAA at https://psl.noaa.gov/data/gridded/data.cpc.globalprecip.html. 850 mb geopotential height, and 850 mb zonal and meridional wind component is obtained from NCEP-NCAR Reanalysis 1 at https://psl.noaa.gov/data/gridded/data.ncep.reanalysis.html. The ETOPO1 data for ice surface versions is obtained from the NOAA at https://www.ncei.noaa.gov/products/etopo-global-relief-model.

Code availability

MATLAB was used for coding and plotting. The code used in this study is available from the corresponding author on reasonable request.

References

1. Kotz, M., Levermann, A. & Wenz, L. The effect of rainfall changes on economic production. *Nature* **601**, 223–227 (2022).
2. Zawilski, M. & Brzezińska, A. Areal rainfall intensity distribution over an urban area and its effect on a combined sewerage system. *Urban Water J.* **11**, 532–542 (2014).
3. Guzman Herrador, B. R. et al. Analytical studies assessing the association between extreme precipitation or temperature and drinking water-related waterborne infections: a review. *Environ. Health* **14**, 1–12 (2015).
4. Keller, S. & Atzl, A. Mapping natural hazard impacts on road infrastructure—the extreme precipitation in baden-württemberg, Germany, June 2013. *Int. J. Disaster Risk Sci.* **5**, 227–241 (2014).
5. Huang, T. et al. Analysis and visualization of natural threats against the security of electricity transmission system. *Scientific Bulletin Electrical Eng. Faculty* **1** https://doi.org/10.1515/sbeef-2016-0019 (2017).
6. Bauer, T., Ingram, V., De Jong, W. & Arts, B. The socio-economic impact of extreme precipitation and flooding on forest livelihoods: evidence from the Bolivian Amazon. *Int. Forestry Rev.* **20**, 314–331 (2018).
7. Liu, Y. et al. Global socioeconomic risk of precipitation extremes under climate change. *Earth's. Future* **8**, e2019EF001331 (2020).
8. Shi, X. et al. Impacts and socioeconomic exposures of global extreme precipitation events in 1.5 and 2.0 c warmer climates. *Sci. Total Environ.* **766**, 142665 (2021).
9. Allen, M. R. & Ingram, W. J. Constraints on future changes in climate and the hydrologic cycle. *Nature* **419**, 224–232 (2002).
10. Yin, J. et al. Thermodynamic driving mechanisms for the formation of global precipitation extremes and ecohydrological effects. *Sci. China Earth Sci.* **66**, 92–110 (2023).
11. Zhang, Y. et al. Skilful nowcasting of extreme precipitation with nowcastnet. *Nature* **619**, 526–532 (2023).
12. Li, W., Gao, X., Hao, Z. & Sun, R. Using deep learning for precipitation forecasting based on spatio-temporal information: a case study. *Clim. Dyn.* **58**, 443–457 (2022).
13. Boers, N., Bookhagen, B., Marwan, N. & Kurths, J. Spatiotemporal characteristics and synchronization of extreme rainfall in South America with focus on the Andes mountain range. *Clim. Dyn.* **46**, 601–617 (2016).
14. Boers, N. et al. Propagation of strong rainfall events from southeastern South America to the central Andes. *J. Clim.* **28**, 7641–7658 (2015).
15. Boers, N. et al. Prediction of extreme floods in the eastern central andes based on a complex networks approach. *Nat. Commun.* **5**, 5199 (2014).
16. Strnad, F. M., Schlör, J., Geen, R., Boers, N. & Goswami, B. Propagation pathways of Indo-Pacific rainfall extremes are modulated by Pacific sea surface temperatures. *Nat. Commun.* **14**, 5708 (2023).
17. Gelbrecht, M., Boers, N. & Kurths, J. Phase coherence between precipitation in South America and Rossby waves. *Sci. Adv.* **4**, eaau3191 (2018).
18. Boers, N. et al. Complex networks reveal global pattern of extreme-rainfall teleconnections. *Nature* **566**, 373–377 (2019).
19. Agarwal, A., Guntu, R. K., Banerjee, A., Gadhawe, M. A. & Marwan, N. A complex network approach to study the extreme precipitation patterns in a river basin. *Chaos* **32**, 013113 (2022).
20. Mondal, S., Mishra, A. K. & Leung, L. R. Spatiotemporal characteristics and propagation of summer extreme precipitation events over United States: A complex network analysis. *Geophys. Res. Lett.* **47**, e2020GL088185 (2020).
21. Wolf, F., Ozturk, U., Cheung, K. & Donner, R. V. Spatiotemporal patterns of synchronous heavy rainfall events in east Asia during the baiu season. *Earth Syst. Dyn.* **12**, 295–312 (2021).
22. Qiao, P. et al. Extreme rainfall synchronization network between southwest China and Asia–Pacific region. *Clim. Dyn.* **57**, 3207–3221 (2021).
23. Vallejo-Bernal, S. M. et al. The role of atmospheric rivers in the distribution of heavy precipitation events over North America. *Hydrol. Earth Syst. Sci.* **27**, 2645–2660 (2023).
24. Wang, C., Gao, S., Liang, L., Deng, D. & Gong, H. Multi-scale characteristics of moisture transport during a rainstorm process in north China. *Atmos. Res.* **145**, 189–204 (2014).

25. Schumacher, R. S. & Rasmussen, K. L. The formation, character and changing nature of mesoscale convective systems. *Nat. Rev. Earth Environ.* **1**, 300–314 (2020).

26. Gimeno, L. et al. Recent progress on the sources of continental precipitation as revealed by moisture transport analysis. *Earth-Sci. Rev.* **201**, 103070 (2020).

27. Dettinger, M. D., Ralph, F. M., Das, T., Neiman, P. J. & Cayan, D. R. Atmospheric rivers, floods and the water resources of California. *Water* **3**, 445–478 (2011).

28. Pu, B. & Cook, K. H. Dynamics of the west African westerly jet. *J. Clim.* **23**, 6263–6276 (2010).

29. Wang, S.-Y., Davies, R. E. & Gillies, R. R. Identification of extreme precipitation threat across midlatitude regions based on short-wave circulations. *J. Geophys. Res.: Atm.* **118**, 11059–11074 (2013).

30. Hoskins, B. J. & Ambrizzi, T. Rossby wave propagation on a realistic longitudinally varying flow. *J. Atmos. Sci.* **50**, 1661–1671 (1993).

31. Lenters, J. & Cook, K. Summertime precipitation variability over South America: Role of the large-scale circulation. *Monthly Weather Rev.* **127**, 409–431 (1999).

32. Seluchi, M. E., Garreaud, R., Norte, F. A. & Saulo, A. C. Influence of the subtropical andes on baroclinic disturbances: A cold front case study. *Monthly Weather Rev.* **134**, 3317–3335 (2006).

33. Ludescher, J. et al. Network-based forecasting of climate phenomena. *Proc. Natl. Acad. Sci.* **118**, e1922872118 (2021).

34. Algarra, I., Eiras-Barca, J., Miguez-Macho, G., Nieto, R. & Gimeno, L. On the assessment of the moisture transport by the great plains low-level jet. *Earth Syst. Dyn.* **10**, 107–119 (2019).

35. Tan, X., Gan, T. Y. & Chen, Y. D. Synoptic moisture pathways associated with mean and extreme precipitation over Canada for summer and fall. *Clim. Dyn.* **52**, 2959–2979 (2019).

36. Guan, H., Zhang, X., Skrzypek, G., Sun, Z. & Xu, X. Deuterium excess variations of rainfall events in a coastal area of south Australia and its relationship with synoptic weather systems and atmospheric moisture sources. *J. Geophys. Res.: Atm.* **118**, 1123–1138 (2013).

37. Liu, B. et al. Global atmospheric moisture transport associated with precipitation extremes: Mechanisms and climate change impacts. *Wiley Interdiscip. Rev.: Water* **7**, e1412 (2020).

38. Algarra, I., Eiras-Barca, J., Nieto, R. & Gimeno, L. Global climatology of nocturnal low-level jets and associated moisture sources and sinks. *Atmos. Res.* **229**, 39–59 (2019).

39. Espinoza, J. C. et al. Rainfall hotspots over the southern tropical Andes: Spatial distribution, rainfall intensity, and relations with large-scale atmospheric circulation. *Water Resour. Res.* **51**, 3459–3475 (2015).

40. Eghdami, M. & Barros, A. P. Extreme orographic rainfall in the eastern andes tied to cold air intrusions. *Front. Environ. Sci.* **7**, 101 (2019).

41. Lavers, D. A. & Villarini, G. The nexus between atmospheric rivers and extreme precipitation across Europe. *Geophys. Res. Lett.* **40**, 3259–3264 (2013).

42. Dunstone, N. et al. Skilful seasonal predictions of summer European rainfall. *Geophys. Res. Lett.* **45**, 3246–3254 (2018).

43. Sutton, R. T. & Dong, B. Atlantic Ocean influence on a shift in European climate in the 1990s. *Nat. Geosci.* **5**, 788–792 (2012).

44. Barton, Y. et al. On the temporal clustering of European extreme precipitation events and its relationship to persistent and transient large-scale atmospheric drivers. *Weather Clim. Extremes* **38**, 100518 (2022).

45. Bedoya-Soto, J. M., Poveda, G., Trenberth, K. E. & Vélez-Upegui, J. J. Interannual hydroclimatic variability and the 2009–2011 extreme ENSO phases in Colombia: from Andean glaciers to Caribbean lowlands. *Theor. Appl. Climatol.* **135**, 1531–1544 (2019).

46. Vavrus, S. J., Wang, F. & Block, P. Rainy season precipitation forecasts in coastal Peru from the north American multi-model ensemble. *Int. J. Climatol.* **42**, 6221–6234 (2022).

47. Xavier, P., Rahmat, R., Cheong, W. K. & Wallace, E. Influence of madden-Julian oscillation on southeast Asia rainfall extremes: observations and predictability. *Geophys. Res. Lett.* **41**, 4406–4412 (2014).

48. Chen, M. et al. Assessing objective techniques for gauge-based analyses of global daily precipitation. *J. Geophys. Res. Atm.* **113**, 1–13 (2008).

49. Gandin, L. S. Objective analysis of meteorological fields. *Q. J. Roy. Meteorol. Soc.* **92**, 447–447 (1966).

50. Sun, Q., Miao, C., Qiao, Y. & Duan, Q. The nonstationary impact of local temperature changes and ENSO on extreme precipitation at the global scale. *Clim. Dyn.* **49**, 4281–4292 (2017).

51. Amante, C. & Eakins, B. W. Etopo1 arc-minute global relief model: procedures, data sources and analysis (2009). https://repository.library.noaa.gov/view/noaa/1163/noaa_1163_DS1.pdf.

52. Quiroga, R. Q., Kreuz, T. & Grassberger, P. Event synchronization: a simple and fast method to measure synchronicity and time delay patterns. *Phys. Rev. E* **66**, 041904 (2002).

Acknowledgements

Author contributions

Kaiwen Li: Design, Methodology, Software, Writing, Visualization. Yu Huang: Design, Discussion, Writing. Kai Liu: Methodology, Discussion, Writing, Review. Ming Wang: Supervision, Design, Methodology, Discussion, Writing, Review, Funding acquisition. Niklas Boers: Supervision, Design, Discussion, Writing. Fenying Cai & Jianxin Zhang: Discussion, Review.

Competing interests

The authors declare no competing interests.

Additional information

Supplementary information The online version contains supplementary material available at https://doi.org/10.1038/s41612-024-00701-6.

Correspondence and requests for materials should be addressed to Ming Wang.

Reprints and permissions information is available at http://www.nature.com/reprints

Publisher's note Springer Nature remains neutral with regard to jurisdictional claims in published maps and institutional affiliations.